applied sciences

MDPI

Article

Methods for Reducing Ring Artifacts in Tomographic Images Using Wavelet Decomposition and Averaging Techniques

Paweł Lipowicz [1,*], Marta Borowska [1,*] and Agnieszka Dardzińska-Głębocka [2]

[1] Institute of Biomedical Engineering, Faculty of Mechanical Engineering, Bialystok University of Technology, Wiejska 45C, 15-351 Bialystok, Poland
[2] Department of Mechanics and Applied Computer Science, Faculty of Mechanical Engineering, Bialystok University of Technology, Wiejska 45C, 15-351 Bialystok, Poland; a.dardzinska@pb.edu.pl
* Correspondence: p.lipowicz@pb.edu.pl (P.L.); m.borowska@pb.edu.pl (M.B.)

Abstract: Computed tomography (CT) is one of the fundamental imaging modalities used in medicine, allowing for the acquisition of accurate cross-sectional images of internal body tissues. However, during the acquisition and reconstruction process, various artifacts can arise, and one of them is ring artifacts. These artifacts result from the inherent limitations of CT scanner components and the properties of the scanned material, such as detector defects, non-uniform distribution of radiation from the source, or the presence of metallic elements within the scanning region. The purpose of this study was to identify and reduce ring artifacts in tomographic images using image decomposition and average filtering methods. In this study, tests were conducted on the effectiveness of identifying ring artifacts using wavelet decomposition methods for images. The test was performed on a Shepp–Logan phantom with implemented artifacts of different intensity levels. The analysis was performed using different wavelet families, and linear approximation methods were used to filter the image in the identified areas. Additional filtering was performed using moving average methods and empirical mode decomposition (EMD) techniques. Image comparison methods, i.e., RMSE, SSIM and MS-SSIM, were used to evaluate performance. The results of this study showed a significant improvement in the quality of tomographic phantom images. The authors obtained more than 50% improvement in image quality with reference to the image without any filtration. The different wavelet families had different efficiencies with relation to the identification of the induction regions of ring artifacts. The Haar wavelet and Coiflet 1 showed the best performance in identifying artifact induction regions, with comparative RMSE values for these wavelets of 0.1477 for Haar and 0.1469 for Coiflet 1. The applied additional moving average filtering and EMD permitted us to improve image quality, which is confirmed by the results of the image comparison. The obtained results allow us to assess how the used methods affect the reduction in ring artifacts in phantom images with induced artifacts.

Keywords: computed microtomography; reconstruction algorithms; ring artifact; wavelet decomposition; artifact reduction technique

Citation: Lipowicz, P.; Borowska, M.; Dardzińska-Głębocka, A. Methods for Reducing Ring Artifacts in Tomographic Images Using Wavelet Decomposition and Averaging Techniques. *Appl. Sci.* **2024**, *14*, 7292. https://doi.org/10.3390/app14167292

Academic Editor: Samuel Cheng

Received: 26 June 2024
Revised: 19 July 2024
Accepted: 14 August 2024
Published: 19 August 2024

1. Introduction

Computed tomography is an increasingly popular imaging technique with applications in the fields of medicine, diagnostics, scientific research and industry. A variety of artifacts arise during tomographic imaging. They are caused by various physical phenomena during the emission of radiation. Ring artifacts are one of the most common artifacts. They arise as a result of imperfections in the detector's pixel elements or fiber optic matrix, or defects on scintillator crystals [1]. Ring artifacts can also result from contamination of any of the previously mentioned elements, as well as various types of drift, for example, thermal drift or drift in the X-ray-gene spectrum [2]. Scintillators are the element located in front of the detector optical fiber matrix and have the function of converting ionizing

radiation into visible or near-visible emission. There are a number of materials that exhibit scintillation properties that can exist in crystalline, liquid or gaseous form.

Optical fibers behind the scintillator direct radiation in the visible spectrum emitted by the scintillator directly to individual pixels located on the CCD or CMOS array of the detector (Figure 1). The attenuation or extinguishing of individual pixels during acquisition causes the formation of artifacts in the image [3].

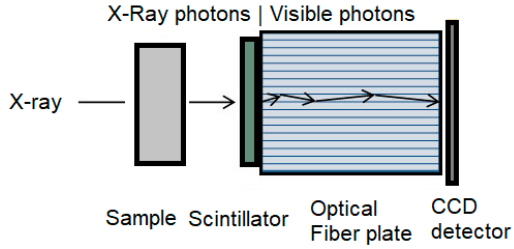

Figure 1. Schematic representation of the structure of the microtomograph's CCD detector, with the X-ray and visible-spectrum radiation areas marked.

Ring artifacts visible on tomograms appear in the form of circles spreading from the center of the image to its edges. There may be several to dozens of them. The visible circles can range in width from single pixels up to several pixels. They can have different grayscale brightness. They significantly affect the qualitative and quantitative analysis of the measured data. They can also distort important morphometric information in the tomographic image. Artifacts hinder such processes as noise reduction, binarization and segmentation in the image [4–7].

Methods for removing these artifacts can be divided into three types: pre-acquisition, pre-reconstruction and post-reconstruction methods. The commonly used pre-acquisition method of reducing ring artifacts resulting from unbalanced detector sensitivity is called flat-field correction. Flat-field correction involves pixel correction so that all pixels have an identical gray value when they are exposed to a beam with specific parameters. These parameters are identical to those used during the acquisition of the research object [8]. In this method, measurement of the bright- and dark-field images is performed. The bright-field image is collected during homogeneous unconstrained radiation of the detector with the X-ray beam, and the dark-field image is the image formed while the radiation is disabled. The correction is calculated as follows for a pixel in the (x, y) position: The intensity of the pixel for the bright field is $I_B(x,y)$, and for the dark field is $I_D(x,y)$, and the average intensity for both fields is μ_B and μ_D. Based on this information, the specific gain of the pixel $G(x,y)$ and the displacement of the pixel $O(x,y)$ can be counted according to the following formula:

$$G(x,y) = \frac{\mu_B - \mu_D}{I_B(x,y) - I_D(x,y)} \quad (1)$$

$$O(x,y) = \mu_B - G(x,y)I_B(x,y) \quad (2)$$

The resulting data can be applied to correct the raw signal $I_{UI}(x,y)$ obtained during acquisition, the result being a corrected pixel value $I_C(x,y)$:

$$I_C(x,y) = I_u(x,y)G(x,y) + O(x,y) \quad (3)$$

The presented method significantly improves image acquisition; however, it does not provide complete removal of ring artifacts [9]. This is due to the nonlinearity of the response function of the photosensitive components of the detector, and to the nonlinearity in time of the uniformity of the radiation beam.

Pre-reconstruction and post-reconstruction methods involve post-acquisition pixel correction. They implement image filtering methods involving entire images or specific areas of artifact occurrence. Pre-reconstruction methods involve translating projections into

sinograms. The damaged area in the sinogram is represented by a darker strip running across all or part of the sinogram. The simplest methods are based on determining the positions of the stripes based on the sum of the pixel values in the image columns. The positions with a sum under a specific threshold are the location of the stripes which then are processed. Such a proposal for artifact reduction is presented in the work of Mark Rivers [10]. This method is effective for very significant artifacts, for example, in the case of damaged pixels. More advanced methods are based on the processing of the obtained sinograms to visualize striations of variable intensity. Well-developed methods use frequency processing using Fourier transform or wavelet decomposition. Such a method is presented in the work of Munch et al., which uses wavelet decomposition and frequency filtering followed by reconstruction to the original sinogram [11]. This method is more efficient; however, it significantly impacts the pixel values within the entire sinogram. The work of Tang et al. presents a hybrid approach to reducing artifacts in the pre-reconstruction process. It involves using wavelet decomposition to identify the positions of artifact induction and then transforming the image within the raw sinogram at predefined positions [12].

The process of reducing artifacts after reconstruction involves transforming tomograms to polar coordinates, identifying artifacts, and removing them using various image processing techniques. In their paper, Sijbers et al. presented such a method using local statistical evaluation of pixel values to identify stripes in a tomogram [13].

In Table 1, the authors present various papers on ring artifact reduction as well. They show on which data the cited methods were tested and present some relevant results of ring artifact reduction if they were presented in the paper.The authors of the paper present a method for pre-reconstruction artifact reduction that uses the identification of artifact induction sites using wavelet decomposition. They apply sinogram processing in two stages to the identified locations and within the entire sinogram. The authors of the current study have developed an original model for reducing ring artifacts using discrete wavelet decomposition supplemented by filtering using empirical mode decomposition (EMD). The authors have not encountered in the literature the use of wavelet decomposition combined with EMD in the filtering of medical tomographic images.

Table 1. A table showing papers on methods for reducing ring artifacts, along with the type of data on which the method was tested and example results.

Authors (year)	Methods	Data	Results
Selim et al. (2022) [14]	Sparsity-based method, during iterative reconstruction algorithms	Real data and simulations	0.9682 (SSIM)
Sijbers et al. (2004) [13]	Post-reconstruction filtration method	Real data	Only visulal results, no quantitative data
Tang et al. (2001) [12]	Wawelet analysis pre-reconstruction method	Callibration cells	Only visulal results, no quantitative data
Kim et al. (2014) [4]	Pre-reconstruction method of calculating the ratio of adjacent detector elements in the projection data, termed the line ratio	Sheep–Logan phantom and human organs models	7.13×10^{-7} (MSE) for Sheep-Logan phantom
Abu et al. (2011) [2]	Comparison five ring artifact removal methods: Modified Wavelet (MWPN) [12], Wavelet-Fourier (WF) method [11], Ring corrections using homogeneity test (RCHT) [13], Ring correction in polar coordinate (RCP) [1], and Strength based ring correction (SBRC) method [15]	Head Phantom and real data	quantitative data for head Phantom (MSSIM): MWPN—0.97 WF—0.81 RCHT—0.82 RCP—0.77 SBRC—0.98

2. Materials and Methods

In this paper, ring artifact reduction was performed on a Shepp–Logan (Yu-Ye-Wang type) tomographic phantom [16]. The phantom was generated at a 512 × 512 × 512 px resolution. All operations, reconstruction and calculations were performed in the Python 3.8 environment with the Tomographic Iterative GPU-based Reconstruction Toolbox (TIGRE toolbox v.2.6) [17]. The python environment uses the libraries NumPy v. 1.21.5 (https://numpy.org, accessed on 20 April 2024), OpenCV v. 4.6.0 (https://opencv.org, accessed on 20 April 2024), Matplotlib v. 3.6.2 [18], PyWavelets v. 1.4.1 [19] and EMD v. 0.5.5 [20]. The development environment was run on a Windows 11 Pro computer equipped with an i7-12700KF 3.60 GHz processor, an NVIDIA GeForce RTX 3070Ti OC 8 GB (New Taipei, Taiwan) graphics card with a 6144 CUDA core, and 64 GB of DDR4 RAM.

After performing ring artifact reduction, the phantom was reconstructed using the FDK algorithm with Shepp–Logan filtering. The process of performing the reconstruction and comparing the results of different reconstruction algorithms with their description was presented in the authors' earlier work [21].

Before performing ring artifact reduction, artifacts were introduced into the generated phantom. Translation of the phantom to sinograms was performed, and 18 stripes with a width of one pixel were introduced at an equal distance from the center of the sinogram (Figure 2). Tests were performed using stripes with values ranging from 2 to 20% larger than the initial grayscale pixel value. Subsequently, all sinograms $S_k(n,j)$ were subjected to discrete two-dimensional first-level wavelet decomposition using wavelets from the "Haar", "Daubechies", "Symlets", "Coiflets", "Biorthogonal" and "Discrete FIR approximation of Mayer wavelet" families. Further analysis was performed on the image after high-pass filtering horizontally scaled and low-pass filtering vertically scaled to the dimensions of the original sinogram [22,23] (Figure 3a).

For each sinogram after decomposition $T_k(n,j)$, the lower b_L and upper b_H levels of the correct pixel values were determined. They were calculated based on the average value of the normalized image of the sinogram before decomposition $w_s = Mean\left(S_k^n(n,j)\right)$, the average standard deviation of the sinogram after decomposition $m_1 = SD(T_k(x,y))$, the average value of the pixels in the image after decomposition $m_2 = Mean(T_k(x,y))$, and a window width factor k selected experimentally. The calculation of the levels of pixel values and binarization follows the following formulas:

$$w_1 = k w_s \sqrt[4]{w_s} \tag{4}$$

$$w_2 = k(0.2 - w_s) \sqrt[4]{w_s} \tag{5}$$

$$b_L = m_1 - w_2 m_2 \tag{6}$$

$$b_H = m_1 + w_1 m_2 \tag{7}$$

$$if\ T_k(n,j) \le b_H\ and\ T_k(n,j) \ge b_L,\ T_k(n,j) = 0; \tag{8}$$

$$if\ T_k(n,j) \le b_L\ and\ T_k(n,j) \ge b_H,\ T_k(n,j) = 1. \tag{9}$$

As a result of these operations, we obtained a matrix of size for image decomposition $T_k(n,j)$ of zeros and ones $B_k(n,j)$ (Figure 3b). The matrix $B_k(n,j)$ was summed with respect to the columns, and the values were divided by the number of rows in the matrix. We obtained a single row matrix $N_k(j) = \frac{\sum_n B_k(n,j)}{n}$. The column positions in the image j of stripe occurrences were identified when $N_k(j) \ge T$, where T is the thresholding level determined experimentally for a particular data set (Figure 4). The positions of artifact occurrences were subjected to local filtering using line interpolation in a window of 0.5% of the image width rounded to the nearest whole odd number, but not less than 3 pixels (pascal). The operation result was a corrected image $S_k''(n,j)$.

(**a**) (**b**)

Figure 2. Reference image of the Shepp–Logan phantom (**a**) and image showing the Shepp–Logan phantom with ring artifacts inserted (**b**).

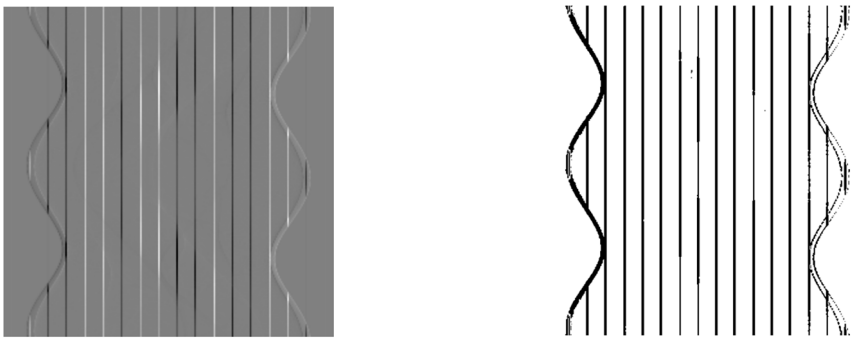

(**a**) (**b**)

Figure 3. The image of the sinogram after wavelet decomposition using the Haar wavelet (**a**) and the result of the binarization process (**b**).

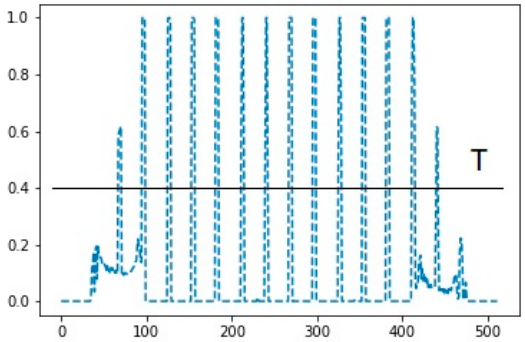

Figure 4. A graph showing the $N_k(j)$ matrix after summing the $B_k(n, j)$ matrix relative to the columns. The T line represents the thresholding level to identify ring artifact stripes.

The use of a certain thresholding level resulted in the fact that the striations with very low intensity below the thresholding level were not identified. This occurred especially in situations where tomography was performed on an element with a very different density. In such a situation, it was proposed to perform additional filtering of the entire sinogram. For this purpose, filtering was performed with moving average [24] methods and using empirical mode decomposition [25,26].

In order to perform the filtering of the moving average, the grayscale values of the pixels of the columns of the corrected sinogram were summed, obtaining the curve $y'(j) =$

$\sum_n S'_k(n,j)$. Then, the curve was filtered according to the formula in Equation (10), and the whole sinogram was multiplied by the correction factor (Equation (11)):

$$y_s(j) = \frac{1}{2N+1}\sum_{k=-N}^{N} y'(j+k). \tag{10}$$

$$S''_k(n,j) = S'_k(n,j)\frac{y_s(j)}{y'(j)}. \tag{11}$$

where N is the span factor.

Global filtering with mask shift EMD was also performed. The exact process and description are presented in the work of Deering et al. [26]. As a result of decomposition to the 4th level, the harmonics of the signal were extracted. The filtered curve $y_s(j)$ was the curve with the highest harmonics removed. The correction process then proceeded according to Equation (11).

The images resulting from the presented processes were subjected to further analysis at a depth of 32 bits. The corrected and reconstructed images were compared with the reference image using image comparison methods. The Root-Mean-Square Error (RMSE) (Equation (12)) [27], Structural Similarity Index (SSIM) (Equations (13) and (14) [28]), and Multi-scale Structural Similarity Index (MS-SSIM) (Equation (15)) [29] methods were used for comparison.

$$RMSE = \sqrt{\frac{1}{M \times N}\sum_{i=0,\ j=0}^{M-1,\ N-1}[k'(i,j) - k(i,j)]^2} \tag{12}$$

where k is the reference image and k' is the corrected image.

$$SSIM(x,y) = [l(x,y)]^{\propto} \cdot [c(x,y)]^{\beta} \cdot [s(x,y)]^{\gamma} \tag{13}$$

$$SSIM(x,y) = \frac{(2\mu_x\mu_y + C_1)(2\sigma_{xy} + C_2)}{\left(\mu_x^2\mu_y^2 + C_1\right)\left(\sigma_x^2\sigma_y^2 + C_2\right)} \tag{14}$$

where C_1 and C_2 are constants using two scalar constants K_1 and K_2 and the dynamic range of the image. In this paper, $K_1 = 0.01$ and $K_2 = 0.03$. The SSIM indexing algorithm uses a sliding window method to evaluate the image quality. SSIM takes values from -1 to 1; $SSIM(x,y) = 1$ if and only if $x = y$. The window is moved pixel by pixel in the whole image. In this paper, the window size is 8×8 px.

$$MS - SSIM(x,y) = [l_M(x,y)]^{\propto_M} \cdot \prod_{j=1}^{M} [c_j(x,y)]^{\beta_j} \cdot [s_j(x,y)]^{\gamma_j} \tag{15}$$

In this paper $K_1 = 0.01$, $K_2 = 0.03$ and the window size is 11×11 px.

3. Results and Discussion

In the first stage, experimental determination of the value of the k-factor was performed. For this purpose, the noisy Shepp–Logan phantom was subjected to wavelet decomposition using a Haar wavelet. A ring artifact reduction process was carried out by changing the value of k in the range from 5 to 35, and the thresholding level was fixed at $T = 0.4$. Global filtering of the whole sinogram was not performed. The reconstruction result was compared to the reference image using the RMSE and MSE methods. The results of the comparison are presented in the graph in Figure 5. The results presented in the graph show the effect of the k parameter on the effectiveness of reducing ring artifacts in the Shepp–Logan phantom image. From the graph, it can be seen that the optimal parameter for this phantom is values above 21. A further increase in the value has no effect on reducing the errors between the reference image and the one obtained as a result of processing and reconstruction.

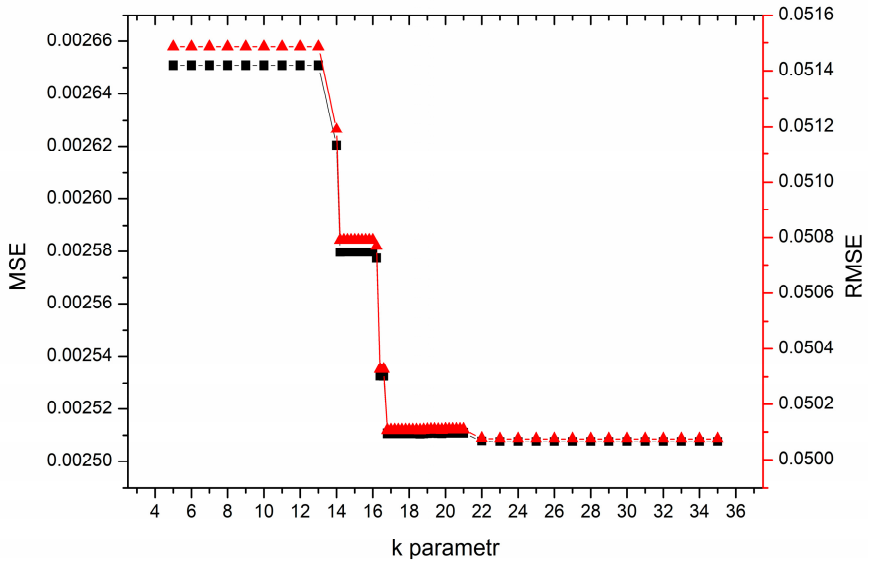

Figure 5. A graph showing the result of comparing images of the reference Shepp–Logan phantom and the reconstructed noisy and filtered image of the Shepp–Logan phantom using the RMSE (red line) and MSE (black line) methods for changing parameter k.

After determining the value of the *k*-factor, the sensitivity of the presented method of reducing ring artifacts to striations of different intensities was checked. For this purpose, the percentage of introduced noise was increased in the range of 2–20%. Reconstruction was performed and the obtained images were compared to the reference image.

Table 2 shows the results of the image comparison for reconstructed images without ring artifact reduction and reconstructed images with artifact reduction. The filtering process used a first-level Haar wavelet, a constant of $k = 21$, a thresholding level of $T = 0.4$ and a span factor of $N = 3$ (Figure 6).The last row of the Table 2 shows the result of comparing the image of the generated phantom and the phantom after reconstruction without introduced artifacts. The analysis of the results presented in the table shows that the reduction in ring artifacts is effective and significantly improves image quality. The results of the MSE method suggest that image noise below 5% as a result of filtering no longer improves image quality. This is due to global filtering, in which, at such a low noise level, the changes resulting from filtering the entire image make more difference than the noise by itself. However, the SSIM and MS-SSIM methods suggest that the filtered image is of similar or even slightly better quality than without filtering at noise levels of 2% AND 5%. With high-intensity stripes, the image has two or even three times the similarity to the reference image.The quantitative results are worse than in the other works cited [2,14], however, it should be noted that in this work the authors use a virtually generated phantom rather than a phantom reconstruction image as a reference image. The filtered back projection (FBP) reconstruction process further introduces some imperfections and simplifications. The work of author Selim M. [14] uses reconstruction and iterative filtering which gives much better results. However, it requires many iterations is much time-consuming and has much higher hardware requirements. The method proposed in this work is much easier to implement and has more practical application today.

Wavelet decomposition was also performed using wavelet families other than the Haar wavelet. This operation was aimed at checking which of the wavelet families used for decomposition would most precisely identify the vertical stripes and separate them from the non-sine data in the sinogram of the reconstructed object. A phantom with a noise level of 10% was subjected to a series of decompositions. After decomposition, it was subjected to a ring artifact reduction process and compared with the reference image. The results for each phantom are recorded in Table 2 and in the graph (Figure 6).

Table 2. Values of calculated similarity coefficients of the post-filtered and noisy unfiltered images of the Sheep-Logan phantom to the reference image.

	PSNR (dB)	MSE	SSIM	MS-SSIM
No Filtration 20% noise	21.99288	0.07074	0.37611	0.60218
Filtered 20% noise	27.09104	0.02187	0.80090	0.82214
No Filtration 10% noise	27.08707	0.02189	0.47612	0.76688
Filtered 10% noise	29.35344	0.01299	0.80226	0.82219
No Filtration 5% noise	34.59004	0.00389	0.61120	0.80143
Filtered 5% noise	27.08509	0.02190	0.80265	0.82261
No Filtration 2% noise	37.74795	0.00188	0.79428	0.88367
Filtered 2% noise	27.09303	0.02186	0.80534	0.82340
Noise-free reconstruction	38.61433	0.00154	0.92164	0.98685

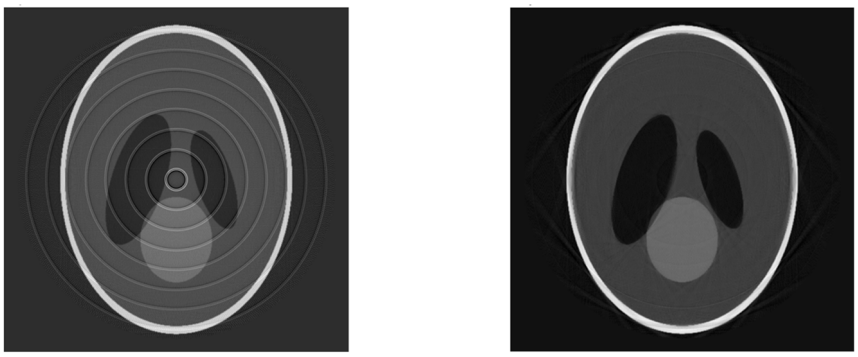

(**a**) (**b**)

Figure 6. Images showing Shepp–Logan phantom reconstructions (**a**) without ring artifact reduction (stripe level 10%) and (**b**) after performing ring artifact reduction with constant k = 21, thresholding level T = 0.4, and span factor N = 3.

When analyzing the results, it should be noted that with the RMSE method, the similarity coefficient tends to 0, so the lower the value, the more similar the obtained image is to the reference image. In the case of the SSIM and MS-SSIM methods, the values tend to 1, that is, the closer the value is to one, the greater the similarity of the images. In the results shown in the Table 3 and Figure 7, you can see four wavelets that obtained significantly higher results than the others: Haar, Coiflet 1, Biorthogonal 2.2 and 3.1 and Daubechies 2. The values of the coefficients are included in Table 3, and the four mentioned wavelets are in bold.

Table 3. Table showing results of comparative analysis of reconstructed images using wavelets of different families and reference image using RMSE, SSIM and MS-SSIM methods. The results with the highest similarity values to the reference image are shown in bold.

Wavelets Type	PSNR (dB)	RMSE	SSIM	MS-SSIM
Haar	29.0471	**0.1477**	**0.8031**	**0.8231**
"Discrete" Meyer	28.9729	0.1502	0.6140	0.7211
Coiflets 1	29.0710	**0.1469**	**0.7898**	**0.8155**
Coiflets 5	29.0279	0.1483	0.6337	0.7244
Coiflets 10	29.,0420	0.1479	0.6533	0.7484
Coiflets 15	29.0320	0.1482	0.6434	0.7320
Biorthogonal 1.5	29.0743	0.1468	0.6708	0.7485
Biorthogonal 2.2	29.0660	**0.1470**	**0.7631**	**0.8052**
Biorthogonal 2.8	29.0713	0.1469	0.6531	0.7320
Biorthogonal 3.1	29.0513	**0.1475**	**0.7833**	**0.8125**
Biorthogonal 3.9	29.0886	0.1463	0.6601	0.7470
Biorthogonal 4.4	29.1073	0.1457	0.7111	0.7823

Table 3. *Cont.*

Wavelets Type	PSNR (dB)	RMSE	SSIM	MS-SSIM
Biorthogonal 5.5	29.0492	0.1476	0.6543	0.7451
Biorthogonal 6.8	29.0364	0.1481	0.6295	0.7083
Daubechies 2	29.0415	**0.1479**	**0.7700**	**0.8080**
Daubechies 10	29.0353	0.1481	0.6633	0.7551
Daubechies 20	29.0182	0.1487	0.6293	0.7366
Daubechies 30	28.9943	0.1495	0.6604	0.7428
Symlets 4	29.0808	0.1465	0.7276	0.7685
Symlets 8	29.0652	0.1471	0.6702	0.7565
Symlets 12	29.0140	0.1488	0.6183	0.7119
Symlets 16	29.0317	0.1482	0.6243	0.7255
Symlets 20	29.0633	0.1471	0.6309	0.7397

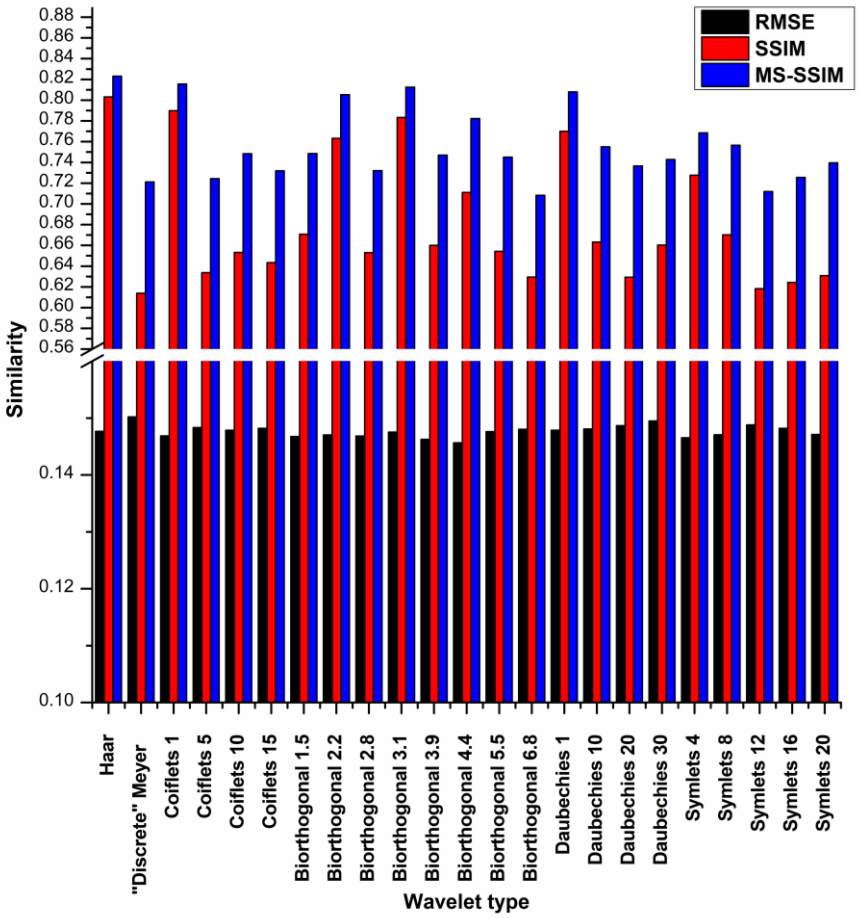

Figure 7. Graph showing results of comparative analysis of images after reconstruction using wavelets of different families and reference image using RMSE, SSIM and MS-SSIM methods.

It can be noted that the more complex the wavelet, the lower the similarity to the reference image obtained. The lowest efficiency was obtained by performing artifact reduction with the "Discrete" Meyers wavelet. The use of global filtering of the entire image may also have affected the values obtained. A slight reduction in the value of all pixels relative to the reference image is visible in the results as a lower similarity even though the morphometric information of the image was not lost.

4. Conclusions

The results presented in this paper show a method of reducing ring artifacts that effectively improves the image in which ring artifacts of different intensities occur. De-

pending on the intensity of the ring artifacts, the results obtained were up to 50% better than the image not subjected to any filtering. The comparison uses a computer-generated cross-sectional image as a reference, rather than a noise-free reconstructed phantom image. This causes the comparison results to be lower, due to the fact that the reconstruction itself introduces other errors and imperfections in the image, not only ring artifacts. The FBP method is not perfect and introduces some approximations to the calculation. The authors made a comparison between the phantom and various reconstruction methods in their earlier paper [21]. The authors intend in this way to show the level of imperfection of the image relative to the real object. An important aspect to pay attention to when performing reduction is the selection of the k parameter. Its imprecise selection can significantly reduce the effectiveness of the method. The need for experimental selection of the parameter k is a drawback of the model; therefore, further research based on varied real data should parametrize this parameter for different materials. A second filtering step based on EMD introduces changes to all pixels in the image, as shown by the comparative results for very slight artifacts (less than 5%). The authors want to conduct further research to develop this method to provide it with more selective performance. Performing a test of different wavelet families in wavelet decomposition showed that the complexity of the wavelet has a negative effect on the effectiveness of artifact reduction. The best results were obtained using the following wavelets: Haar, Coiflet 1, Biorthogonal 2.2 and 3.1 and Daubechies 2. The lowest efficiency was obtained by performing artifact reduction with the "Discrete" Meyers wavelet. Greater variation in the results for individual wavelets is expected when reducing ring artifacts in real images due to the greater complexity of such images. This type of work is planned in further work on artifact reduction in tomographic images. The authors are in the process of testing the method on real data obtained from the micro-CT Skyscan 1172, and the results of this work will be presented in the authors' next article.

Author Contributions: Conceptualization, P.L., M.B. and A.D.-G.; methodology, P.L. and M.B.; software, P.L.; validation, P.L. and M.B.; formal analysis, M.B. and A.D.-G.; investigation, P.L.; resources, P.L.; data curation, P.L.; writing—original draft preparation, P.L.; writing—review and editing, M.B. and A.D.-G.; visualization, P.L.; supervision, M.B.; project administration, P.L.; funding acquisition, P.L. All authors have read and agreed to the published version of the manuscript.

Funding: This work was supported by the Ministry of Science and Higher Education of Poland under research project No. WI/WM-IIB/8/2023.

Institutional Review Board Statement: Not applicable.

Informed Consent Statement: Not applicable.

Data Availability Statement: This paper did not use external data; phantom images and artifacts were generated in software. Source codes can be made available by email after contacting the corresponding author.

Conflicts of Interest: The authors declare no conflicts of interest.

References

1. Kyriakou, Y.; Prell, D.; Kalender, W.A. Ring artifact correction for high-resolution micro CT. *Phys. Med. Biol.* **2009**, *54*, N385–N391. [CrossRef] [PubMed]
2. Anas, E.M.; Kim, J.G.; Lee, S.Y.; Hasan, K. Comparison of ring artifact removal methods using flat panel detector based CT images. *Biomed. Eng. Online* **2011**, *10*, 72. [CrossRef] [PubMed]
3. Kalender, W.A.; Kyriakou, Y. Flat-detector computed tomography (FD-CT). *Eur. Radiol.* **2007**, *17*, 2767–2779. [CrossRef] [PubMed]
4. Kim, Y.; Baek, J.; Hwang, D. Ring artifact correction using detector line-ratios in computed tomography. *Opt. Express* **2014**, *22*, 13380–13392. [CrossRef]
5. Çimen, T.; Düzgün, S.; Akyüz, İ.E.; Topçuoğlu, H.S. The effect of cone beam computerized tomography voxel size and the presence of root filling on the assessment of middle mesial canals in mandibular molar teeth. *Clin. Oral Investig.* **2024**, *28*, 394. [CrossRef] [PubMed]
6. Hiller, J.; Hornberger, P. Measurement accuracy in X-ray computed tomography metrology: Toward a systematic analysis of interference effects in tomographic imaging. *Precis. Eng.* **2016**, *45*, 18–32. [CrossRef]

7. Pauwels, R.; Stamatakis, H.; Bosmans, H.; Bogaerts, R.; Jacobs, R.; Horner, K.; Tsiklakis, K. Quantification of metal artifacts on cone beam computed tomography images. *Clin. Oral Implant. Res.* **2013**, *24*, 94–99. [CrossRef] [PubMed]
8. Kwan, A.L.; Seibert, J.A.; Boone, J.M. An improved method for flat-field correction of flat panel X-ray detector. *Med. Phys.* **2006**, *33*, 391–393. [CrossRef] [PubMed]
9. Lifton, J.; Liu, T. Ring artefact reduction via multi-point piecewise linear flat field correction for X-ray computed tomography. *Opt. Express* **2019**, *27*, 3217–3228. [CrossRef]
10. Rivers, M. Tutorial Introduction to X-ray Computed Microtomography Data Processing. Available online: https://www.mcs.anl.gov/research/projects/X-ray-cmt/rivers/tutorial.html (accessed on 7 December 2023).
11. Munch, B.; Trtik, P.; Marone, F.; Stampanoni, M. Stripe and ring artifact removal with combined wavelet—Fourier filtering. *Opt. Express* **2009**, *17*, 8567–8591. [CrossRef]
12. Tang, X.; Ning, R.; Yu, R.; Conover, D. Cone beam volume CT image artifacts caused by defective cells in x-ray flat panel imagers and the artifact removal using a wavelet-analysis-based algorithm. *Med. Phys.* **2001**, *28*, 812–825. [CrossRef] [PubMed]
13. Sijbers, J.; Postnov, A. Reduction of ring artefacts in high resolution micro-CT reconstructions. *Phys. Med. Biol.* **2004**, *49*, N247. [CrossRef] [PubMed]
14. Selim, M.; Rashed, E.A.; Atiea, M.A.; Kudo, H. Sparsity-based method for ring artifact elimination in computed tomography. *PLoS ONE* **2022**, *17*, e0268410. [CrossRef] [PubMed]
15. Anas, E.M.A.; Lee, S.Y.; Hasan, M.K. Removal of ring artifacts in CT imaging through detection and correction of stripes in the sinogram. *Phys. Med. Biol.* **2010**, *55*, 6911. [CrossRef] [PubMed]
16. Yu, H.; Ye, Y.; Wang, G. Katsevich-type algorithims for variable radius spiral cone-beam CT. In Proceedings of the Developments in X-Ray Tomography IV, Bellingham, WA, USA, 26 October 2004; pp. 550–557.
17. Biguri, A.; Dosanjh, M.; Hancock, S.; Soleimani, M. TIGRE: A MATLAB-GPU toolbox for CBCT image reconstruction. *Biomed. Phys. Eng. Express* **2016**, *2*, 055010. [CrossRef]
18. Hunter, J.D. Matplotlib: A 2D Graphics Environment. *Comput. Sci. Eng.* **2007**, *9*, 90–95. [CrossRef]
19. Lee, G.; Gommers, R.; Waselewski, F.; Wohlfahrt, K.; O'Leary, A. PyWavelets: A Python package for wavelet analysis. *J. Open Source Softw.* **2019**, *4*, 1237. [CrossRef]
20. Quinn, A.; Lopes-Dos-Santos, V.; Dupret, D.; Nobre, A.; Woolrich, M. EMD: Empirical Mode Decomposition and Hilbert-Huang Spectral Analyses in Python. *J. Open Source Softw.* **2021**, *6*, 2977. [CrossRef]
21. Lipowicz, P.; Dardzińska-Głębocka, A.; Borowska, M.; Biguri, A. Comparison of Analytical and Iterative Algorithms for Reconstruction of Microtomographic Phantom Images and Rat Mandibular Scans. In *Information Technology in Biomedicine, Proceedings of the 9th International Conference, Kamień Śląski, Poland, 20–22 June 2022*; Springer Nature: Cham, Switzerland, 2022; pp. 107–118.
22. Mallat, S.; Hwang, W.L. Singularity detection and processing with wavelets. *IEEE Trans. Inf. Theory* **1992**, *38*, 617–643. [CrossRef]
23. Toufik, B.; Mokhtar, N. The wavelet transform for image processing applications. *Adv. Wavelet Theory Their Appl. Eng. Phys. Technol.* **2012**, *17*, 395–422.
24. Boin, M.; Haibel, A. Compensation of ring artefacts in synchrotron tomographic images. *Opt. Express* **2006**, *14*, 12071–12075. [CrossRef] [PubMed]
25. Huang, N.E.; Shen, Z.; Long, S.R.; Wu, M.C.; Shih, H.H.; Zheng, Q.; Yen, N.-C.; Tung, C.C.; Liu, H.H. The empirical mode decomposition and the Hilbert spectrum for nonlinear and non-stationary time series analysis. *Proc. R. Soc. Lond. Ser. A Math. Phys. Eng. Sci.* **1998**, *454*, 903–995. [CrossRef]
26. Deering, R.; Kaiser, J.F. The use of a masking signal to improve empirical mode decomposition. In Proceedings of the (ICASSP '05) IEEE International Conference on Acoustics, Speech, and Signal Processing, 2005, Philadelphia, PA, USA, 23–23 March 2005; Volume 484, pp. iv/485–iv/488.
27. Asamoah, D.; Ofori, E.; Opoku, S.; Danso, J. Measuring the performance of image contrast enhancement technique. *Int. J. Comput. Appl.* **2018**, *181*, 6–13. [CrossRef]
28. Wang, Z.; Bovik, A.C.; Sheikh, H.R.; Simoncelli, E.P. Image quality assessment: From error visibility to structural similarity. *IEEE Trans. Image Process* **2004**, *13*, 600–612. [CrossRef] [PubMed]
29. Wang, Z.; Simoncelli, E.P.; Bovik, A.C. Multiscale structural similarity for image quality assessment. In Proceedings of the Thrity-Seventh Asilomar Conference on Signals, Systems & Computers, 2003, Pacific Grove, CA, USA, 9–12 November 2003; pp. 1398–1402.